nature chemistry

Article

https://doi.org/10.1038/s41557-025-01827-7

Interfacial assembly of biomimetic MOF-based porous membranes on coacervates to build complex protocells and prototissues

Received: 2 March 2024

Accepted: 11 April 2025

Published online: 4 June 2025

Check for updates

Yanglimin Ji [1,2], Yiyang Lin [3] & Yan Qiao [1,2]

The bottom-up construction of cell-like entities or protocells is essential for emulating cytomimetic behaviours within artificial cell consortia. Complex coacervate microdroplets are promising candidates for primordial cells; however, replicating the complex cellular organization and cell–cell interactions using membraneless coacervates remains a major challenge. To address this, we developed membrane-bound coacervate protocells by interfacial assembly of metal–organic framework nanoparticles around coacervate microdroplets. By leveraging the inherently porous structure and surface chemistry of metal–organic frameworks, we demonstrated the ability to regulate biomolecular organization within the protocells and integrate proteins into the membrane, thereby imitating both integral and peripheral membrane proteins. These membranized coacervates were further engineered into artificial-organelle-incorporated protocells and tissue-like assemblies capable of signal processing and protocell-to-protocell communication. Our findings highlight the potential of designing artificial systems with spatially controlled biomolecular organization to mimic natural cellular functions, paving the way for the assembly of membranized coacervates into prototissues.

The pursuit of creating synthetic cells with authentic structure and functionality poses a considerable challenge in the fields of synthetic biology, bioengineering and the study of life's origin[1,2]. Dynamic microcompartmentalized entities, known as protocells, including vesicles[3,4], polymersomes[5–7], proteinosomes[8,9], colloidosomes[10–12], emulsion droplets[13–16] and capsules[17,18], have been designed to imitate cytomimetic behaviours such as cell growth[19,20], division[21,22], motion[23–25], communication[26,27] and enzymatic metabolism[28,29]. Apart from membrane-enclosed synthetic cells, membraneless coacervate microdroplets arising from liquid–liquid phase separation have been extensively explored as protocell models to study the origin of life[30–33]. These membraneless microcompartments contain liquid-like microphases, enabling the enrichment of biomolecules[34,35], the formation of chemical gradients[36] and the confinement of complex biochemical reactions[37–39]. The study of coacervation is also motivated by the existence of intracellular membraneless organelles or biomolecular condensates, which act as active or repressive hubs for intracellular storage and signalling[40,41].

[1]Beijing National Laboratory for Molecular Sciences (BNLMS), Laboratory of Polymer Physics and Chemistry, CAS Research/Education Center for Excellence in Molecular Sciences, Institute of Chemistry, Chinese Academy of Sciences, Beijing, China. [2]University of Chinese Academy of Sciences, Beijing, China. [3]State Key Laboratory of Chemical Resource Engineering, Beijing Laboratory of Biomedical Materials, Beijing University of Chemical Technology, Beijing, China. e-mail: yanqiao@iccas.ac.cn

https://doi.org/10.1038/s41557-025-01827-7

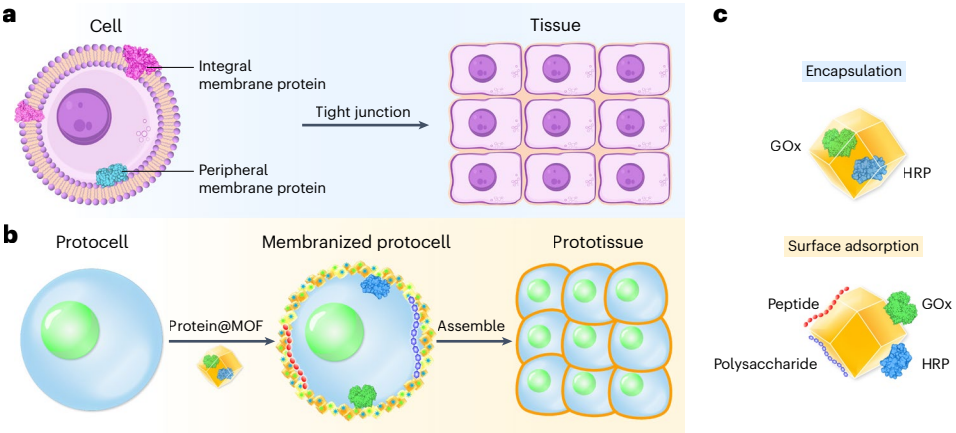

Fig. 1 | Hierarchical organization and assemblage of natural cells and protocells. a, Schematic illustration of a cell containing plasma membrane, cytoplasm and organelles. Cellular adhesion and organization lead to the formation of tissue with tight cellular connections. **b**, Schematic of a multiphase coacervate protocell, which is further protected with a layer of MOF nanoparticles. The membranized coacervates can be assembled into tissue-like entities. **c**, Two modes of MOF–biomolecule interactions: biomolecular encapsulation and surface adsorption.

Unlike membrane-bound protocells, membraneless coacervates have demonstrated the ability to sequester a broad range of molecules from their surrounding environment[42]. However, their selectivity for biomolecular enrichment is relatively low. Additionally, coacervate microdroplets tend to coalesce to minimize interfacial energy[43], which makes it difficult to develop prototissues or communicating protocells in contact mode. It is therefore important to design stable protocell coacervates capable of selectively recruiting biomolecules from their environment. To achieve this, a variety of membranization methods have been developed using fatty acids[44], phospholipids[45], block copolymers[46], protein–polymer conjugates[47,48], polysaccharides[49], nanoparticles[50] and cell fragments[51,52]. Despite these advances, a considerable challenge remains in developing coacervate-based protocells that can organize biomolecules at different scales, enabling the localization of biomolecules, biological interactions and biochemical reactions. In biology, cells have evolved hierarchically complex structures for regulating biomolecular organization such as intracellular organelles for protein localization and the plasma membrane for hosting membrane proteins[53]. However, the bottom-up fabrication of protocell coacervates incorporating biomimetic localization of membrane proteins remains an unachieved goal.

Inspired by hierarchical cellular organization, including structures such as the cytomembrane, cytoplasm and organelles, along with their complex functions (Fig. 1a), we aim to achieve functional membranization of coacervate microdroplets as advanced protocells. This approach is designed to enable controlled semipermeability, protocellular communication and multitiered organization. Our strategy utilizes the interfacial assembly of metal–organic frameworks (MOFs) to create a protective layer featuring intrinsic cavities and unique surface chemistry (Fig. 1b). This design facilitates additional compartments that regulate biomolecular organization through encapsulation and surface binding. It allows for the incorporation of proteins into the MOF membrane, thereby mimicking the location of both integral and peripheral proteins (Fig. 1c). Integral proteins are embedded within the lipid bilayer and span the entire membrane, while peripheral proteins are loosely attached to the exterior or interior surfaces of the membrane. We further investigate the potential of developing organelle-embedded protocells and tissue-like structures with MOF-membranized coacervates capable of protocellular communication and spatially controlled cascade enzyme reactions.

Results and discussion

Membranization of coacervate protocells with MOF

As a protocell model, complex coacervate microdroplets consisting of poly(diallyldimethylammonium chloride) (PDDA) and poly(acrylic acid) (PAA) (total monomer concentration, 12.5 mM; molar ratio, 1:1) were prepared (Fig. 2a). The cell-sized coacervates were further coated with a layer of zeolitic-imidazolate framework-8 (ZIF-8, ~60 nm in diameter; Supplementary Fig. 1). This process was accomplished through the direct interfacial self-assembly of ZIF-8 on coacervate droplets, driven by the multivalent interactions such as electrostatic attraction and metal–ligand coordination between the locally exposed zinc ions and PAA. These interactions also led to a reduction in the interfacial tension of MOF-coated coacervates ($\gamma_{MOF\text{-}coac} = 0.14$ mN m^{-1}), compared with that of PDDA/PAA coacervates ($\gamma_{coac} = 0.38$ mN m^{-1}) (Fig. 2b). Additionally, steric hindrance due to the large particle size of the MOFs prevented the penetration of MOF nanoparticles into the coacervate lumen, thereby playing a crucial role in the interfacial assembly. According to $\Delta G = \pi R^2 \gamma_{coac}(1 - |\cos\theta_{MOF\text{-}coac}|)^2$[54] where $R = 30$ nm is the radius of ZIF-8, and $\theta_{MOF\text{-}coac} = 129.1°$ is the wetting angle of the coacervates on MOF-coated glass surface (Fig. 2c), the free energy required to remove ZIF-8 from the coacervate surface (that is, ΔG) is calculated to be 5.4×10^{-19} J, which is two orders of magnitude greater than the energy of colloidal particles in Brownian motion or the kinetic energy of ZIF-8 nanoparticles ($E_k = kT$, 4×10^{-21} J). This result indicated that the detachment of ZIF-8 from the coacervate interface was energetically unfavourable. The zeta potentials of ZIF-8 and coacervates were measured to be +26.3 ± 1.7 mV and +33.7 ± 3.6 mV, respectively, indicating that electrostatic attraction alone was not the primary factor driving MOF assembly (Supplementary Fig. 2). To further investigate the role of electrostatic interactions in membranization, we adjusted the surface charges of PDDA/PAA coacervates and ZIF-8 nanoparticles. Increasing the proportion of polycations resulted in more positively charged PDDA/PAA coacervates (2:1; zeta potential, +41.6 ± 5.5 mV), which failed to form a membrane with the positively charged ZIF-8 (Supplementary Fig. 3). This trend was also observed with supplementary PDDA/PAA ratios of 5:4, 7:6 and 8:7 (Supplementary Fig. 4). Conversely, the negatively charged PDDA/PAA coacervates (zeta potentials, −39.2 ± 3.8 mV, −42.1 ± 3.5 mV and −45.7 ± 2.8 mV for ratios of 1:2, 1:3 and 1:4, respectively) induced the aggregation of positively charged ZIF-8. Furthermore, negatively charged ZIF-8 (−11.1 ± 1.5 mV) was encapsulated by oppositely charged coacervates (1:1), while forming a continuous membrane on the negatively charged coacervates (1:1.5, −18.9 ± 3.5 mV). These results indicated that adequate electrostatic repulsion between the coacervates and MOF nanoparticles was essential for successful membranization. Isothermal titration calorimetry was performed to demonstrate the affinity of PAA for ZIF-8 nanoparticles with an equilibrium dissociation constant (K_d) of $1.32 \pm 0.71 \times 10^{-4}$ M, indicative of an intermediate affinity (Supplementary Fig. 5). Additionally, lysine

https://doi.org/10.1038/s41557-025-01827-7

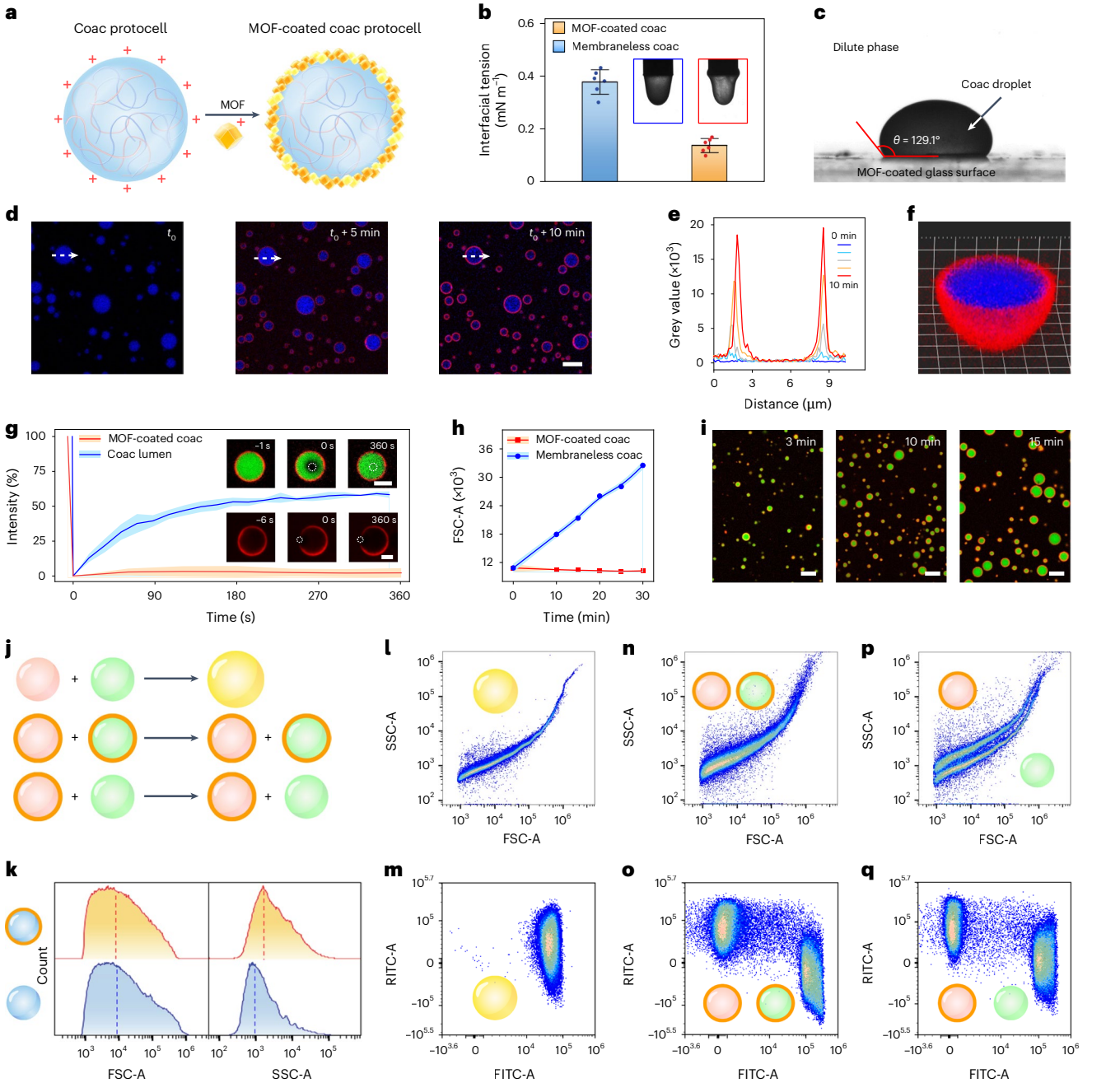

Fig. 2 | Stabilizing coacervate microdroplets via membranization with MOF nanoparticles. a, Scheme illustrating the assembly of the ZIF-8 nanoparticles on PDDA/PAA coacervates. **b**, Interfacial tension of PDDA/PAA droplets in the coacervate dilute phase without (blue bar) and with (orange bar) a ZIF-8 membrane exhibited a decrease from 0.38 to 0.14 mN m^{-1}. The error bars represent the mean ± s.d. of six replicates. **c**, Determination of the wetting angle of a coacervate droplet on the surface of a ZIF-8-coated glass. The surrounding medium was the coacervate dilute phase. **d**, Time-dependent fluorescence microscopy images illustrating the self-assembly process of RhB@ZIF-8 nanoparticles (final concentration, 4 mg ml^{-1}; red) onto the PDDA/PAA coacervates (final concentration, 12.5 mM; molar ratio, 1:1; blue) to form continuous membranes. The coacervates were doped with fluorescent PAA (labelled with DL405). Scale bar, 10 μm. **e**, Time-lapse line-scan analysis of red fluorescence intensity across the MOF-membranized coacervates in **d**, as indicated by white arrows. **f**, Reconstructed 3D image of a coacervate microdroplet (doped with DL405-PAA) coated with RhB@ZIF-8. Grid width, 2 μm. **g**, Time-lapse fluorescence microscopy images (insets) and corresponding fluorescence intensity curves showing fluorescence recovery of FITC-PEI in the coacervate lumen and MOF membrane after photobleaching, suggesting 60% and negligible recovery of fluorescence intensity within 360 s, respectively. Scale bars, 5 μm. **h**, Time-dependent FSC median increased continuously for membraneless coacervates (blue line), while remaining unchanged over a period of 30 min for MOF-coated coacervates (red line). The error bands in **g**,**h** represent the mean ± s.d. of three replicates. **i**, Fluorescence microscopy images of membrane-bound coacervates incubated for 3, 10 and 15 min before mixing with ZIF-8 dispersions. The median diameter grew with the increase of incubation time. Scale bars, 10 μm. **j**, Schematic illustration of the structural stability of mixed binary coacervate populations. The red and green spheres represent droplet protocells encapsulating different fluorescent payloads, while the yellow sphere represents a protocell formed after droplet fusion. **k**, FSC-A and SSC-A histograms for the PDDA/PAA coacervates before and after MOF coating, showing that the SSC median for MOF-coated coacervates (red dashed lines) was twofold higher than membraneless coacervates (blue dashed lines), respectively. **l**–**q**, 2D pseudocolour plots of FSC versus SSC (**l**,**n**,**p**) and FITC versus rhodamine B isothiocyanate (RITC) (**m**,**o**,**q**) for the mixed binary populations of TAMRA-ssDNA or FITC-PEI containing membraneless coacervates (**l**,**m**), TAMRA-ssDNA- or FITC-PEI-doped MOF-coated coacervates (**n**,**o**), and TAMRA-ssDNA-doped MOF-coated coacervates and FITC-PEI-doped membraneless coacervates (**p**,**q**). The coating of MOF membrane on the coacervates prevented droplet fusion and payload exchange. coac, coacervate.

was utilized as a competitive ligand to disrupt the Zn–PAA coordination, leading to the disassembly of the MOF layer (Supplementary Fig. 6). The membranization of coacervates was also accomplished using ZIF-90, which was formed by Zn^{2+} and imidazole-2-carboxaldehyde (zeta potential, 11.4 ± 3.5 mV; mean diameter, 800 nm), underscoring the versatility of this method (Supplementary Fig. 7).

We then applied confocal laser scanning microscopy (CLSM) to capture the real-time images of the membranization process and observed an increase in interfacial fluorescence from ZIF-8 nanoparticles (loaded with rhodamine B (RhB)) (Fig. 2d,e and Supplementary Video 1). A reconstructed three-dimensional (3D) image revealed a continuous membrane of ZIF-8 nanoparticles on the surface of coacervate microdroplets (Fig. 2f). We implemented fluorescence recovery after photobleaching (FRAP) to investigate the structural characteristics of membranized coacervates. To this end, we doped fluorescein isothiocyanate–polyethylenimine (FITC-PEI) into RhB@MOF-stabilized PDDA/PAA coacervates. After photobleaching the lumen of coacervates, the fluorescence intensity recovered to 60% of the original level within 280 s, indicating a liquid-like property with an apparent diffusion coefficient of 3.6×10^{-14} m^2 s^{-1} (Fig. 2g). In contrast, unlike fluidic lipid membranes, the RhB@MOF membrane behaved like a solid phase, showing no noticeable fluorescence recovery after photobleaching[45]. Additionally, the MOF-coated coacervates showed a spherical capsule structure under scanning electron microscopy, formed by the closely packed MOF nanoparticles (Supplementary Fig. 8).

Membraneless coacervates are known to grow in size via coalescence[55]. Having demonstrated the interfacial assembly of ZIF-8, we further examined the colloidal stability of complex coacervates with flow cytometry, where the forward scattered light (FSC) medians of membraneless coacervates exhibited a threefold increase after incubation for 30 min (Fig. 2h). In contrast, the FSC of membranized coacervates remained unchanged. This result suggested that the size of membraneless coacervates increased with time, whereas MOF-protected coacervates remained unchanged. This was confirmed by fluorescence microscopy, in which the former grew to ~4.6 μm (median) after a 30-min incubation, whereas the latter did not change its size (Supplementary Fig. 9). Building on this finding, we then prepared membranized coacervates with controlled size (for example, 1.60 ± 0.06 μm, 2.28 ± 0.06 μm and 2.74 ± 0.11 μm in diameter) by adding MOF particles to coacervates at different time points (Fig. 2i).

We further studied the effect of membranization on the structural stability of coacervates in consortia of two populations by separately loading carboxytetramethylrhodamine (TAMRA)-ssDNA and FITC-PEI into membraneless coacervates and MOF-bound coacervates (Fig. 2j). A flow cytometry study of a single coacervate population demonstrated a similar FSC median. Side-scattered light (SSC), however, which measures the scatter at 90°, depends on the multiple refraction of light through intracellular compartments—and thus correlates to the granularity, internal structure and membrane roughness of the protocell[56]—displayed a twofold increase in median for membranized compared with membraneless coacervates, implying an increase in complexity after membranization (Fig. 2k and Supplementary Fig. 10). Mixing the binary protocell populations of membraneless coacervates resulted in coalescence and payload mixing (Fig. 2l,m and Supplementary Fig. 11a,b). In contrast, binary systems containing two populations of MOF-membranized coacervates remained stable and separated (Supplementary Fig. 11c,d), displaying similar scattering patterns (SSC and FSC) but distinct fluorescence intensities (Fig. 2n,o). Additionally, we observed the coexistence of a mixture of MOF-coated coacervates (doped with TAMRA-ssDNA) and membraneless coacervates (doped with FITC-PEI) without droplet coalescence or payload exchange (Fig. 2p,q and Supplementary Fig. 11e,f). Upon extending the mixing time, we found that MOF-coated coacervates could isolate their payloads for over 48 h (Supplementary Fig. 12).

Regulating biomolecular localization in membranized coacervate protocells

Spatial organization is a hallmark of all living systems. Porous ZIF-8 nanoparticles offered two approaches to localize biomolecules[57]. In strategy I, we exploited the interfacial MOF layer as an absorbing hub to selectively localize biomolecules (e.g., proteins, DNA and polypeptides) and polymers on the surface of coacervates. This effect was believed to arise from the multivalent interactions between the exposed surface of ZIF-8 and the biomolecules through electrostatic attraction (for example, zinc–carboxylate) and coordination bonding (for example, zinc–amine). We initially encapsulated different cargoes inside coacervates and assembled ZIF-8 on the surface. The migration and localization of cargoes were recorded under a microscope. Typically, the guest molecules with a high charge density and a high molecular weight were retained in the coacervate lumen, whereas those compounds with a low charge density or a low molecular weight were found to migrate from the coacervate lumen to the MOF membranes (Fig. 3a,b). For example, upon membranization, ssDNA was retained in the coacervate lumen, while horseradish peroxidase (HRP) was mostly adsorbed by the ZIF-8 layer (Supplementary Fig. 13). Dextran sulfate was found to partially migrate to the MOF membrane. This phenomenon was also observed with polylysine (PLys) of various molecular weights (that is, 15–30 kDa, 4–15 kDa and 1–5 kDa), where PLys with a high molecular weight was mostly trapped in the coacervate lumen, and small polypeptides were absorbed by the MOF layer (Fig. 3c–e). Similar results were also observed with a range of compounds (Supplementary Figs. 14 and 15 and Supplementary Table 1).

In strategy II, the interfacial MOF served as an adsorptive and permeable layer to recruit guest molecules from the external surrounding environment, in which large molecules adsorbed on the outer surface while highly charged small molecules diffused into the coacervate lumen (Fig. 3f). Small molecules with low charge density were distributed at both the coacervate lumen and MOF layer. We summarized these findings in a distribution diagram (Fig. 3g, Supplementary Fig. 16 and Supplementary Table 2), in which PLys was sequestrated by the MOF layer (Fig. 3h), HPTS was located both on the MOF layer and within the coacervate lumen (Fig. 3i), while PEI was confined to the coacervate lumen (Fig. 3j). Our results suggested a molecular weight cut-off of approximately 5 kDa for biomolecules to penetrate through the MOF membrane. Additionally, we modulated the membrane thickness by varying the concentration of MOFs. The average thickness of the MOF membrane increased from 0.33 μm to 0.54 μm, 0.61 μm and 0.64 μm as the MOF concentration increased from 2.66 mg ml^{-1} to 4.00 mg ml^{-1}, 5.33 mg ml^{-1} and 6.66 mg ml^{-1}, respectively (Supplementary Fig. 17). Notably, a thicker MOF membrane exhibited a lower permeability, with a molecular-weight cut-off decreasing from approximately 15 kDa to 1 kDa for membranes of 0.61 μm and 0.64 μm thickness, respectively (Supplementary Fig. 18).

In biology, the plasma membrane is a highly dynamic and flexible lipid bilayer, described as fluid mosaic model. Membrane proteins can be associated with the lipid bilayer in different ways. Integral membrane proteins are inserted into the plasma membrane via hydrophobic interactions, while peripheral membrane proteins interact with the surface of the lipid bilayer without entering into the hydrophobic core. The diffusion of negatively charged biomolecules (for example, DNA) through the hydrophobic lipid bilayer is generally restricted. In our study, the MOF membrane exhibited solid-like characteristics with lower fluidity (Fig. 2g and Supplementary Table 3), which facilitated the selective penetration of biomolecules, with a molecular-weight cut-off of approximately 5 kDa when the membrane thickness was 0.61 μm (Supplementary Fig. 17). Unlike lipid bilayers, the proteins on MOF membranes do not readily mimic transmembrane structures or function. Also, the diffusion of encapsulated biomolecules within the cavity of MOF membrane is slow. We developed two approaches to achieve protein organization within protocells (Supplementary Fig. 19): (1) encapsulating concanavalin A (ConA) inside ZIF-8 on the membrane; (2) adsorbing ConA to the inner surface of the MOF membrane.

https://doi.org/10.1038/s41557-025-01827-7

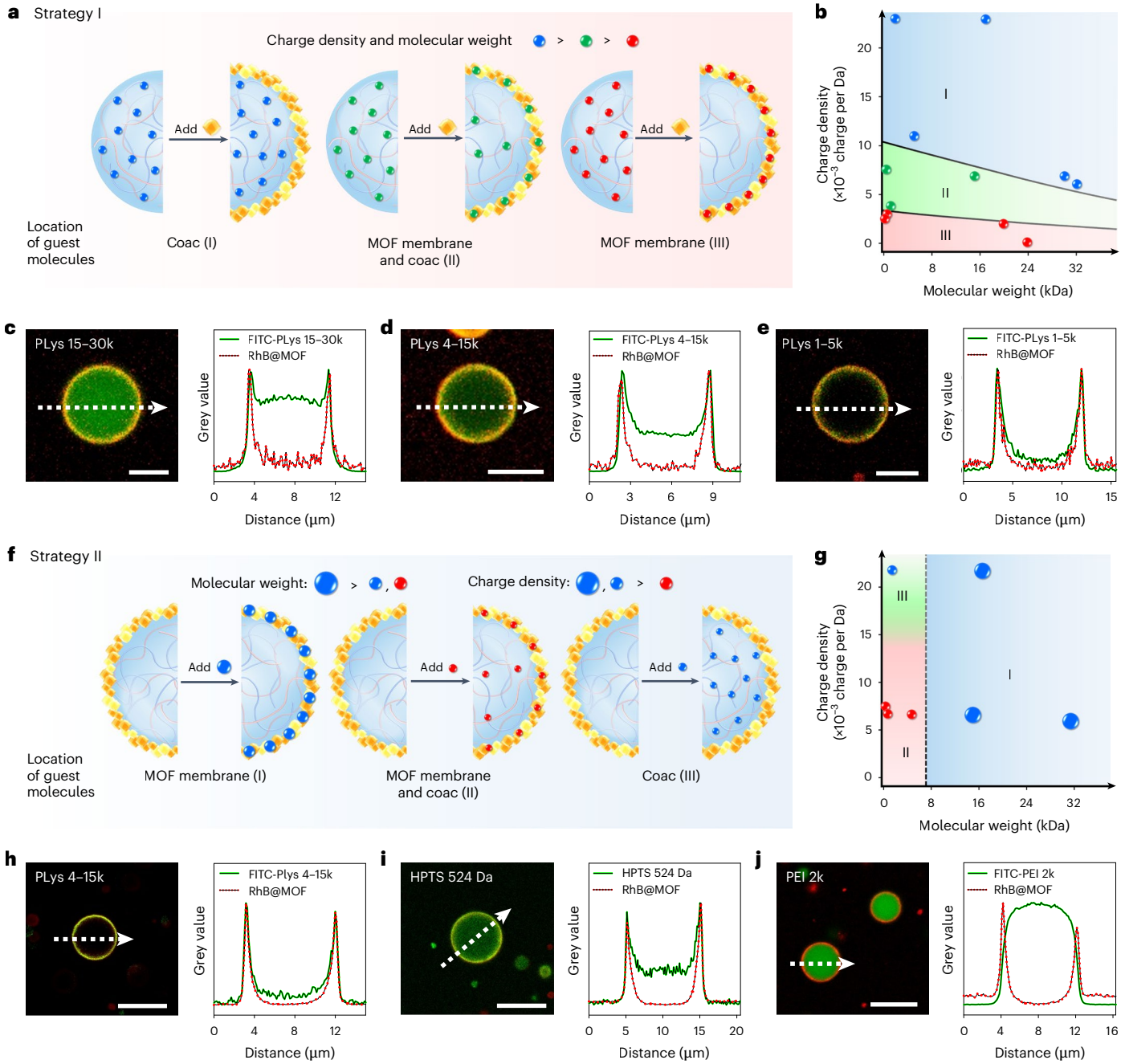

Fig. 3 | Regulating the spatial distribution of guest molecules with an MOF membrane. Guest molecules were preloaded in coacervates followed by MOF membranization (strategy I, **a**–**e**), or added into MOF-coated coacervate dispersions (strategy II, **f**–**j**). **a**, Schematic illustration of strategy I, in which guest molecules relocated from the coacervate lumen to the MOF membrane as the charge density was reduced and the molecular weight was lowered. **b**, Following strategy I, the distribution of cargoes was summarized according to **c**–**e** and Supplementary Figs. 13–15. **c**–**e**, CLSM images and corresponding line-scan analysis (red dotted lines for RhB@MOF, green solid lines for fluorescent molecules) of FITC-PLys with molecular weights of 15–30 kDa (**c**), 4–15 kDa (**d**) and 1–5 kDa (**e**) in MOF-coated coacervates. PLys with larger molecular weights tended to locate in the coacervate lumen, whereas smaller PLys preferentially adsorbed onto MOF membrane. Scale bars, 10 μm. **f**, Schematic illustration of strategy II, in which the MOF membrane adsorbed large molecules but permitted the penetration of molecules with low molecular weight and high charge density. Cargoes with a low charge density were distributed both in the lumen and on the surface. **g**, Following strategy II, the spatial distribution of cargoes was summarized according to **h**–**j** and Supplementary Fig. 16. **h**–**j**, Fluorescence microscopy images and corresponding line-scan analysis (red dotted lines for RhB@MOF, green solid lines for fluorescent molecules) of FITC-PLys with a molecular weight of 4–15 kDa (**h**), HPTS with a molecular weight of 524 Da (**i**) and FITC-PEI with a molecular weight of 2 kDa (**j**) in MOF-coated coacervates. Scale bars, 10 μm. The grey values in panels **c**,**d**,**e**,**h**,**i** and **j** were normalized to 1. The coloured spheres represent the guest molecules with different charge density and molecular weights.

Regulated spatial localization of enzymatic reactions

Having demonstrated the regulation of biomolecular organization, we sought to compartmentalize enzymes and catalytic biochemical reactions within complex coacervates. To achieve this, we exploited MOF nanoparticles as a hub to modulate the distribution of enzymes.

In case I, enzyme cascades involving glucose oxidase (GOx) and HRP were separately encapsulated within ZIF-8, preserving their catalytic activity and allowing substrates and reaction products to diffuse through the porous frameworks (Supplementary Fig. 20). Transmission electron microscopy analysis confirmed the successful encapsulation of proteins

https://doi.org/10.1038/s41557-025-01827-7

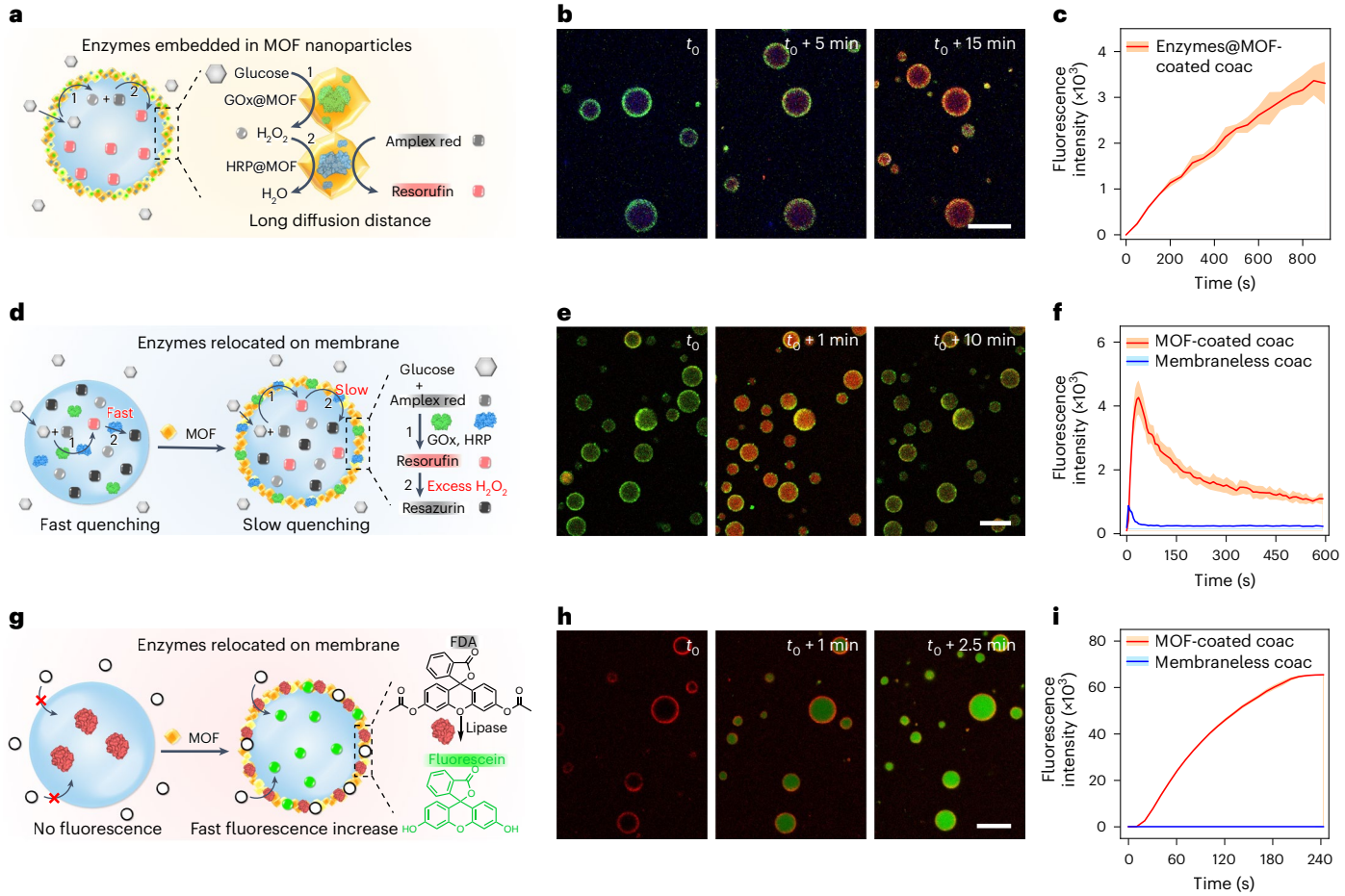

Fig. 4 | Spatial regulation of enzymatic reactions by MOF membrane. **a**–**c**, Schematic illustration (**a**), CLSM images (**b**) and corresponding fluorescence intensity change (**c**) for the GOx- and HRP-catalysed oxidation of Amplex red, where the enzymes were embedded in the MOF nanoparticles. With the addition of glucose, the Amplex red was oxidized into resorufin, emitting red fluorescence. For imaging, GOx and HRP were partially labelled with FITC and DL405, respectively. **d**–**f**, Scheme (**d**), CLSM images (**e**) and corresponding fluorescence intensity changes (**f**) for the GOx- and HRP-mediated oxidation of Amplex red in membraneless (blue line) and membrane-bound coacervates (**e**, red line). The Amplex red underwent fast oxidation to red-fluorescent resorufin and further to non-fluorescent resazurin in membraneless coacervates. In MOF-coated coacervates, the transient fluorescence from resorufin was stronger and more persistent. For imaging, GOx was partially labelled with FITC. **g**–**i**, Schematic image (**g**), fluorescence microscopy images (**h**) and corresponding fluorescence intensity change curves (**i**) for the lipase-mediated FDA lysis in membraneless (blue line) and membrane-bound coacervates (**h**, red line). The hydrophobic FDA molecules were not sequestrated by the lipase-doped membraneless coacervates. The presence of interface MOF was able to enrich lipase, enabling lipase-catalysed FDA hydrolysis and a rapid increase in green fluorescence. The error bands in **c**,**f**,**i** represent the mean ± s.d. of three replicates. Scale bars, 10 μm.

within ZIF-8 nanoparticles. Specifically, calcining HRP@ZIF-8 at 325 °C for 2 h effectively removed HRP, resulting in cavities within the ZIF-8 nanoparticles (Supplementary Fig. 21)[58]. These enzyme-encapsulated MOFs were then assembled on the surface of PDDA/PAA complex coacervates. The HRP-substrate Amplex red was loaded into coacervate microdroplets, after which glucose was added to initiate the GOx-catalysed oxidation of glucose to gluconic acid, resulting in the formation of hydrogen peroxide as a by-product (Fig. 4a). In the presence of HRP, this intermediate product was able to oxidize Amplex red into the fluorescent product resorufin. Indeed, we observed a continuous increase in red fluorescence from resorufin across the coacervate microdroplets (Fig. 4b,c). The reaction rate was relatively low, probably due to the long diffusion distance required for substrates to penetrate the MOF nanoparticles to reach the embedded enzymes[57,59].

In case II, the interfacial MOF layer was able to relocate the enzymes inside coacervates via multivalent interactions, allowing for the modulation of the catalytic reaction rate. To prove this, we encapsulated cascade enzymes (that is, GOx and HRP) within complex coacervates and compared the reaction rate with and without MOF membranization (Fig. 4d). As shown in Fig. 4e, we observed the emergence of red fluorescence from the product of resorufin in MOF-coated coacervates, resulting from the cascade reactions as discussed above. This fluorescence was observed to fade rapidly (Fig. 4e,f) due to the oxidation of resorufin into non-fluorescent resazurin by the accumulated hydrogen peroxide (Supplementary Video 2)[60]. In membraneless coacervates, the lifetime of red fluorescence was shorter and its transient intensity was much lower (Supplementary Fig. 22a and Supplementary Video 3). We hypothesized that the membranization of coacervates absorbed enzymes to the surface, down-regulating the rate of catalytic reaction and the generation of hydrogen peroxide. As such, we observed an intensified red fluorescence with a longer lifetime (Fig. 4e,f).

In case III, we showed that the interfacial MOF layer was able to trigger a catalytic reaction that was inhibited in membraneless coacervates. In this experiment, we encapsulated lipase inside coacervates and fed its substrate fluorescein diacetate (FDA) to the solution, in which we did not observe the generation of the product fluorescein (Fig. 4g, Supplementary Fig. 22b and Supplementary Video 4). This was because hydrophobic FDA was not able to diffuse into the highly hydrated core of coacervates. By contrast, the adsorption of ZIF-8 on the surface was observed to trigger the catalytic reaction, leading to a continuous

increase in the green fluorescence within coacervates (Fig. 4h,i). This was due to the MOF-mediated localization of lipase on the surface of coacervates, which facilitated the enzyme–substrate interaction and the enzymatic reaction (Fig. 4h,i and Supplementary Video 5).

Artificial-organelle-embedded multicompartmentalized coacervate protocells

To mimic the hierarchical organization of natural cells, we sought to construct multiphase coacervates within MOF-coated coacervates. To this end, liquid-like PDDA/PAA coacervates (total concentration, 12.5 mM; molar ratio, 1:1) were designed as the cytoplasm that sequestrated protamine/folic acid coacervate microdroplets (Prot/FA; total concentration, 0.25 mM; molar ratio, 3:1) as the artificial organelles (Fig. 5a). The high efficacy of loading artificial organelles within membraneless coacervate protocells was demonstrated from CLSM and the interfacial assembly of MOF nanoparticles on coacervates was illustrated by a reconstructed 3D image (Fig. 5b–d). Flow cytometry was used to statistically reveal the stepwise assembly of PDDA/PAA coacervates (Fig. 5e), Prot/FA@PDDA/PAA coacervates (Fig. 5f) and MOF-coated Prot/FA@PDDA/PAA coacervates (Fig. 5g), in which the SSC increased from 1,200 to 3,000 and 7,000 (Fig. 5h), respectively, suggesting the elevated structural complexity of protocells.

Furthermore, this strategy was highly adaptable for designing versatile hierarchical protocells with various inner liquid-like coacervates (Fig. 5i). For example, we demonstrated the replacement of Prot/FA organelles with Prot/DNA (total concentration, 1.7 mg ml^{-1}; mass ratio, 17:10), resulting in the formation of MOF-coated Prot/DNA@PDDA/PAA protocells (Fig. 5j). Interestingly, we were able to create vesicle-like organelles inside coacervate protocells by adjusting the proportion of Prot/FA organelles (total concentration, 0.25 mM; molar ratio, 10:1) (Fig. 5k)[61,62]. Additionally, the PDDA/PAA complex coacervates were loaded with Prot/FA coacervates (total concentration, 0.25 mM; molar ratio, 3:1) as artificial organelles, with GOx or HRP sequestered within them, respectively (Fig. 5l). We also examined the ability of these artificial organelles in MOF-coated multicompartmentalized coacervates to retain their payloads, which remained unexchanged for approximately 16 h (Supplementary Fig. 23).

Having established the artificial-organelle-containing MOF-coated coacervates, we sought to achieve the regulation of chemical reaction cascades by spatially localizing enzymes within subcompartments and adjusting the diffusion permeation of substrates through the MOF membrane. To this end, three cascade enzymes of amylase, GOx and HRP were selectively incorporated into protocells, where amylase was preloaded in the PDDA/PAA coacervates and GOx/HRP were in the Prot/FA coacervates. As illustrated in Fig. 5m, the membranization of Prot/FA@PDDA/PAA multiphase coacervates resulted in enzyme redistribution, in which amylase was adhered to the MOF membrane (Supplementary Fig. 24) and GOx/HRP were retained in the Prot/FA organelles (system I). In this system, the amylase adsorbed on the MOF membrane catalysed the hydrolysis of amylose into glucose. Following the catalytic reaction, the product glucose diffused into the embedded Prot/FA coacervates. As a result, the encapsulated GOx catalysed the oxidation of glucose in the presence of oxygen, leading to the generation of gluconic acid and hydrogen peroxide. In the presence of encapsulated HRP, the latter product further oxidized Amplex red into red-fluorescent resorufin (Fig. 5n,o and Supplementary Video 6). In comparison, system II was designed to contain mixed binary populations of the membranized PDDA/PAA coacervates with amylase binding to the MOF layer and Prot/FA coacervates sequestrating GOx and HRP. In the cascade reaction, the glucose generated by the amylase@MOF-coated coacervates diffused into Prot/FA coacervate population, stimulating the catalytic cascade reaction to generate red-fluorescent resorufin (Fig. 5n,p and Supplementary Video 7). Compared with system II, system I showed more rapid signal amplification. This was because the multicompartmentalized coacervates facilitated cascade reactions within the coacervates themselves, thereby overcoming diffusion limitations[63,64]. In the control experiment with binary populations of membraneless PDDA/PAA and Prot/FA coacervates, the cascade reaction was slower than both system I and II (Fig. 5n and Supplementary Fig. 25). This can be attributed to the absence of the colocalization effect of the MOF membrane.

Tissue-like protocell organization

The biological function of tissues relies on the collective and coordinated behaviours of cells[65]. We showed that MOF-coated protocells were able to assemble into tissue-like structures by shielding electrostatic repulsion between interfacial MOF membranes (Fig. 6a). With the addition of sodium chloride, the MOF-coated coacervates adhered to the neighbouring microdroplets, generating structurally stable prototissues (Fig. 6b, Supplementary Fig. 26 and Supplementary Video 8). The MOF layer between two adhered protocells was thicker than the original ones, which possibly underwent fusion and interfacial rearrangement, causing a subsequent decrease in the layer thickness (Supplementary Fig. 27). The interfacial MOF layers were calculated to be 1.2–1.5 times thicker, causing an increase in the stiffness of the membrane and the generation of non-spherical protocells. This strategy enabled the construction of versatile prototissues, such as a single population of artificial-organelle-containing MOF-coated coacervates (Fig. 6c and Supplementary Fig. 28), binary populations of membranized TAMEA-ssDNA or FAM-ssDNA-doped coacervates (Fig. 6d), and binary populations of organelle-containing membranized coacervates and organelle-free coacervates (Fig. 6e). We further examined the effect of metal ions on the assembly of MOF-coated coacervates. The increase in concentration of sodium chloride to 1 M disassembled the MOF membrane and induced the coalescence of coacervates (Supplementary Fig. 29a), while a lower concentration (50 mM) of sodium chloride cannot trigger the formation of prototissues (Supplementary Fig. 29b). Moreover, sodium sulfate triggered the assembly of MOF-coated coacervates into prototissues with discontinuous membranes due to the stronger electrostatic interaction from anions (Supplementary Fig. 30a), while magnesium ions were found to cause vacuolization due to the strong binding to PAA (Supplementary Fig. 30b,c).

The chemical communication among the microcompartments within prototissues was subsequently investigated with ternary populations of coacervate protocells. As shown in Fig. 6f, artificial-organelle-containing coacervate protocells were developed by loading Prot/FA coacervates into PDDA/PAA coacervates. Specifically, three cascade enzymes of β-galactosidase (β-gal), GOx and HRP were separately doped in artificial organelles. Subsequently, the outer coacervates were protected with a ZIF-8 layer (Fig. 6f,h). The addition of substrate lactose triggered the cascade reactions by enabling chemical communications between different coacervates. Initially, lactose crossed the MOF membrane and diffused into Prot/FA coacervates, resulting in the formation of glucose. This product diffused into a neighbouring coacervate containing GOx, which catalysed the oxidation of glucose into gluconic acid and hydrogen peroxide. Similarly, hydrogen peroxide further diffused into a neighbouring PDDA/PAA coacervate encapsulating HRP to activate the oxidation of Amplex red into resorufin, which diffused back to the other populations of coacervates (Fig. 6f). In a different scenario, three cascade enzymes of β-gal, GOx and HRP were separately relocated on the MOF membrane, which was used to protect coacervates and develop prototissues (Fig. 6g,i). For both systems, an increase in red fluorescence intensity was observed after the addition of lactose, suggesting the successful signal processing between different microcompartments (Supplementary Fig. 31 and Supplementary Videos 9 and 10). It is noteworthy that the increase of red fluorescence intensity was faster in the prototissue with relocated enzymes on the membrane than in prototissue with artificial organelles, which was attributed to the lower diffusion limit of signalling molecules (Fig. 6j).

https://doi.org/10.1038/s41557-025-01827-7

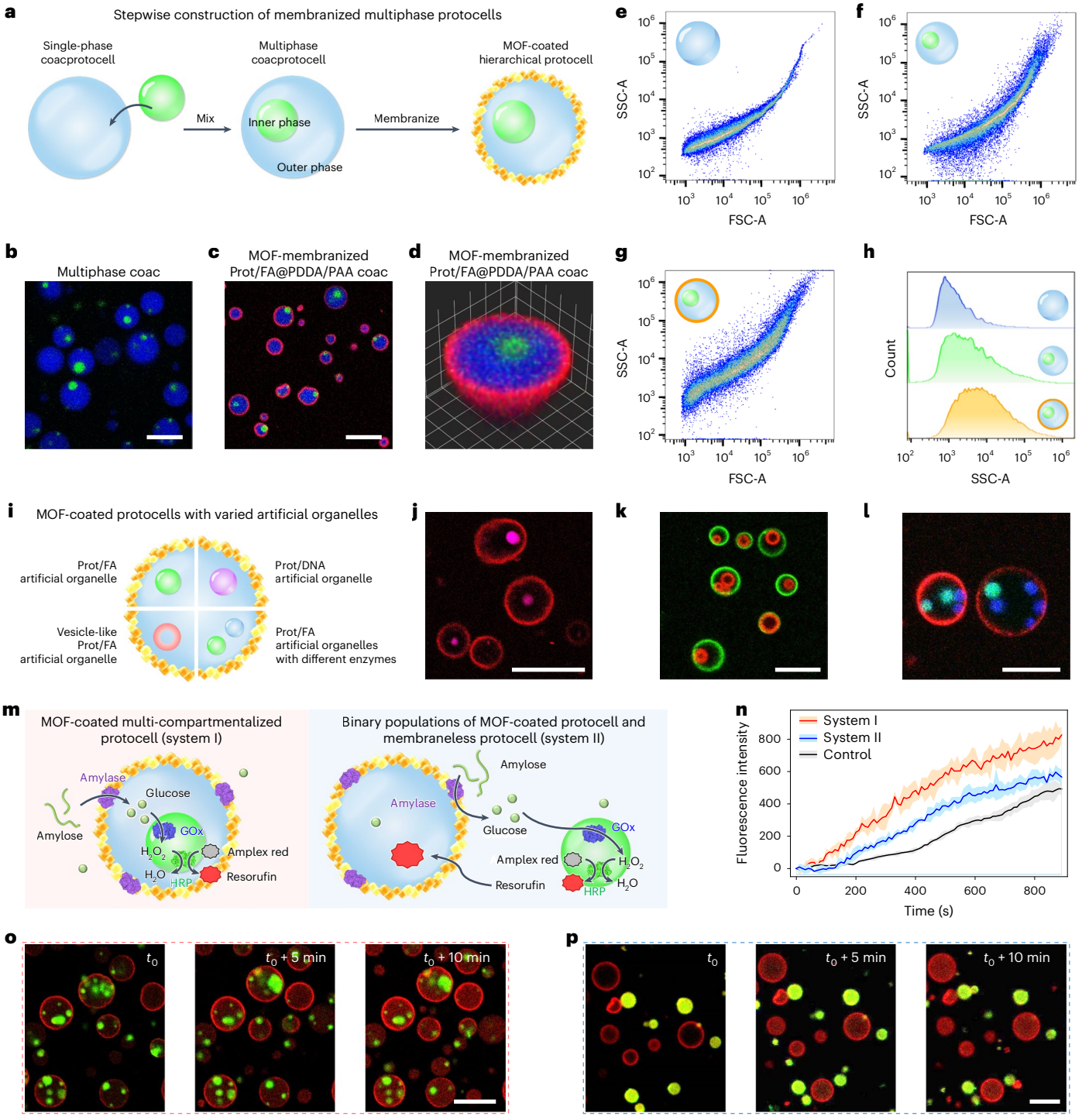

Fig. 5 | Construction of artificial-organelle-containing membrane-bound multicompartmentalized coacervate protocells. a, Scheme for the assembly of artificial-organelle-containing membranized coacervates. **b**–**d**, Fluorescence microscopy images (**b**,**c**) and reconstructed 3D image (**d**) of the Prot/FA@PDDA/PAA multiphase coacervates (**b**) and RhB@ZIF-8-protected Prot/FA@PDDA/PAA coacervates (**c**,**d**). Prot/FA was doped with Cy5-HRP (green), while PDDA/PAA coacervates were loaded with FITC-PEI (blue). Grid width, 1 µm. **e**–**h**, Two-dimensional pseudocolour plots of FSC versus SSC (**e**–**g**) and SSC histograms (**h**) for membraneless single-phase coacervates (**e**,**h**), membraneless multiphase coacervates (**f**,**h**) and membrane-bound multicompartmentalized coacervates (**g**,**h**). **i**–**l**, Scheme (**i**) and CLSM images (**j**–**l**) for MOF-membranized multicompartmentalized coacervates with various artificial organelles: Prot/DNA coacervate organelles (Prot/DNA phase dyed with FAM-ssDNA, MOF membrane labelled with RhB@MOF) (**j**), Prot/FA coacervate vesicle-like organelles (red autofluorescence from FA, MOF membrane doped with fluorescein) (**k**) and binary populations of Prot/FA coacervate organelles (Prot/FA phase doped with Cy5-HRP or FITC-GOx, MOF membrane labelled with RhB@MOF) (**l**). **m**, Schematic illustration of the spatially regulatory cascade enzymatic reaction in MOF-coated multicompartmentalized coacervates (system I) and chemical communication between MOF-coated PDDA/PAA coacervates and membraneless Prot/FA coacervates (system II). **n**–**p**, Time-dependent fluorescence intensity (**n**) and CLSM images (**o**,**p**) showing the faster generation of red-fluorescent resorufin in system I (red curve, **o**) than in system II (blue curve, **p**) and a control experiment of membraneless multiphase coacervates (black curve, Supplementary Fig. 25). The error bands represent the mean ± s.d. of three replicates. Scale bars, 10 µm.

https://doi.org/10.1038/s41557-025-01827-7

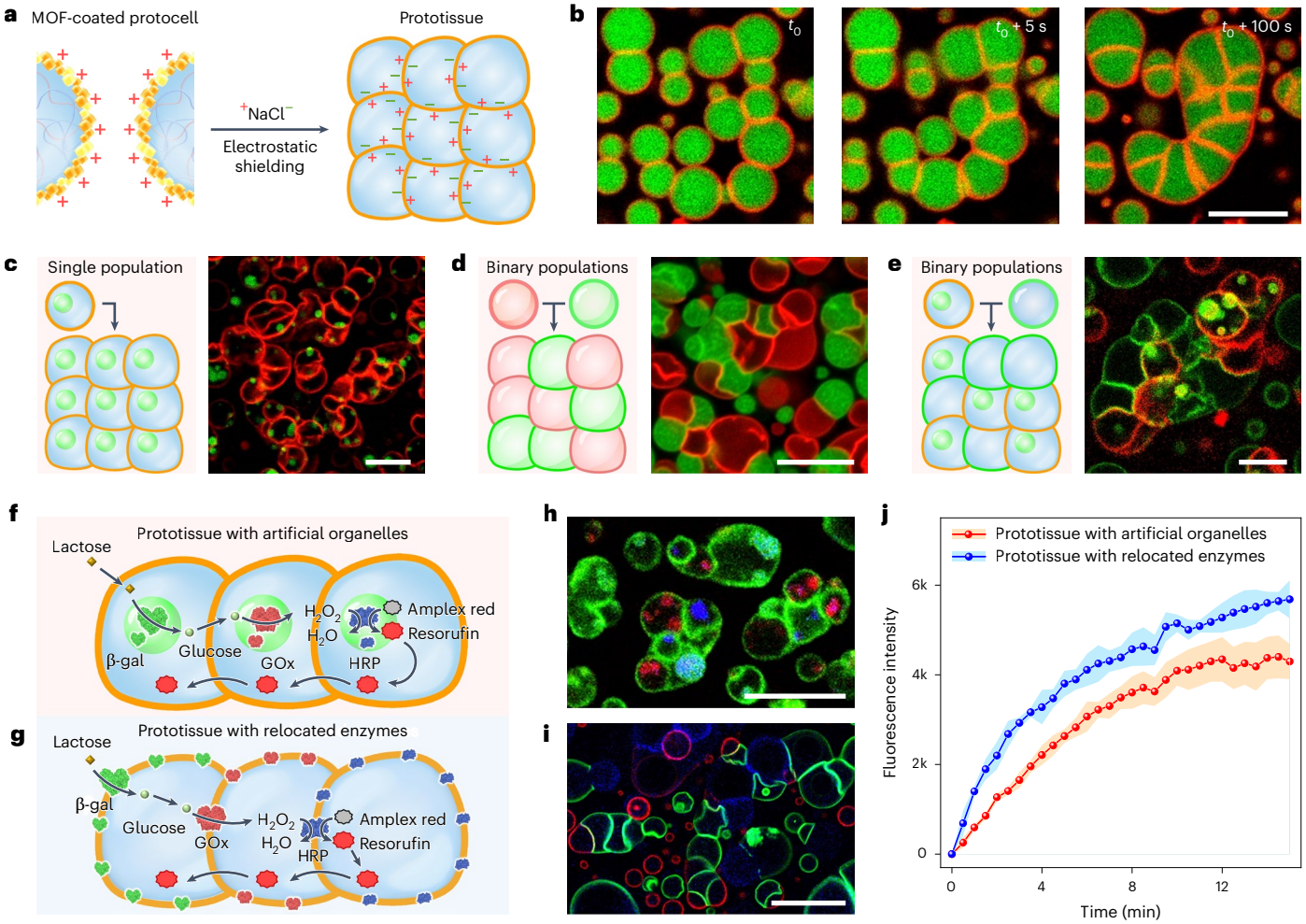

Fig. 6 | Protocellular assembly into tissue-like assemblage. a,**b**, Schematic illustration (**a**) and time-lapse CLSM images (**b**) of sodium-chloride-induced assembly of MOF-membranized coacervate protocells towards prototissue via shielding the electrostatic repulsion. For fluorescence imaging, MOF was doped with RhB, and PDDA/PAA coacervates were doped with FITC-PEI. The adjacent MOF-coated coacervate microdroplets adhered to each other and formed a closely packed tissue-like structure after adding sodium chloride. **c**–**e**, Schematic images and CLSM images for the distinct prototissues constructed with a range of components: organelle-containing RhB@MOF-membranized FITC-Prot/FA@PDDA/PAA coacervates (**c**), binary populations of MOF-membranized PDDA/PAA coacervates loaded with FAM-ssDNA and TAMRA-ssDNA, respectively (**d**), and binary populations of FITC-BSA@MOF-membranized coacervates and RhB@MOF-coated FITC-Prot/FA@PDDA/PAA coacervates (**e**). Scale bars, 5 μm. **f**,**g**, Schematic illustration of enzymatic-cascade-reaction-mediated chemical communication in prototissues: β-gal, GOx and HRP were separately loaded in the artificial organelles of three populations of coacervates (**f**); β-gal, GOx and HRP were separately encapsulated in the porous MOF membrane of three populations of coacervates (**g**). **h**,**i**, Fluorescence images of the prototissues with enzyme-containing artificial organelles (**h**) and prototissue with relocated enzymes on MOF membrane (**i**). β-Gal and GOx were labelled with FITC and RITC, respectively. HRP was labelled with Cy5 and DL405 in **h**,**i**, respectively. MOF was loaded with fluorescein in **h**.**j**, Time-dependent fluorescence intensity showing the production of red-fluorescent resorufin in prototissues. The error bands represent the mean ± s.d. of three replicates. Scale bars, 10 μm.

Conclusions

In this work, we developed a platform to design membranized coacervate protocells capable of biomolecular organization, signal processing and prototissue formation. We achieved this by leveraging the interfacial assembly of intrinsically porous MOF nanoparticles into a semipermeable membrane on complex coacervates. This membrane both provided a physical barrier, which prevented coacervate coalescence, and enhanced colloidal stability, thereby increasing the structural complexity of the coacervates. The MOF membrane functioned as a hub to regulate the spatial distribution of biomolecules, either by encapsulating them within the structure or by enriching them on the surface, analogous to the location of membrane proteins. Utilizing the hierarchically structured protocells, composed of a solid-like MOF membrane, coacervate-based cytoplasm and embedded organelles, we demonstrated the construction of complex protocell systems capable of chemical communication and signal processing. Furthermore, we highlighted the creation of prototissues through the salt-induced assembly of MOF-coated coacervates via electrostatic shielding, which facilitated enzymatic reaction-driven signal communication among microcompartments within the prototissues. Despite the success of salt-induced formation of prototissue, external manipulation (for example, centrifugation) or surface-chemistry-enabled colloid recognition can be implemented to further increase the spatial control and effectiveness of protocell assembly. We anticipate that this work will provide a versatile platform for designing cell mimics with life-like behaviours and will advance the fundamental study of protocells and prototissues. For example, such systems can be used as cell-cluster-like models and instigate the diffusion and supply of essential nutrients and oxygen to cells within the organoid.

Online content

Any methods, additional references, Nature Portfolio reporting summaries, source data, extended data, supplementary information, acknowledgements, peer review information; details of author contributions

and competing interests; and statements of data and code availability are available at https://doi.org/10.1038/s41557-025-01827-7.

References

1. Mann, S. Systems of creation: the emergence of life from nonliving matter. *Acc. Chem. Res.* **45**, 2131–2141 (2012).
2. Guindani, C., Brunsveld, L. C., Cao, S., Ivanov, T. & Landfester, K. Synthetic cells: from simple bio-inspired modules to sophisticated integrated systems. *Angew. Chem. Int. Ed.* **61**, e202110855 (2022).
3. Liu, L. et al. Enzyme-free synthesis of natural phospholipids in water. *Nat. Chem.* **12**, 1029–1034 (2020).
4. Elani, Y., Law, R. V. & Ces, O. Vesicle-based artificial cells as chemical microreactors with spatially segregated reaction pathways. *Nat. Commun.* **5**, 5305 (2014).
5. Rifaie-Graham, O. et al. Photoswitchable gating of non-equilibrium enzymatic feedback in chemically communicating polymersome nanoreactors. *Nat. Chem.* **15**, 110–118 (2023).
6. Sun, J. et al. Morphogenesis of starfish polymersomes. *Nat. Commun.* **14**, 3612 (2023).
7. Liu, G. et al. Oscillating the local milieu of polymersome interiors via single input-regulated bilayer crosslinking and permeability tuning. *Nat. Commun.* **13**, 585 (2022).
8. Gobbo, P. et al. Programmed assembly of synthetic protocells into thermoresponsive prototissues. *Nat. Mater.* **17**, 1145–1153 (2018).
9. Huang, X. et al. Interfacial assembly of protein–polymer nano-conjugates into stimulus-responsive biomimetic protocells. *Nat. Commun.* **4**, 2239 (2013).
10. Rodriguez-Arco, L., Li, M. & Mann, S. Phagocytosis-inspired behaviour in synthetic protocell communities of compartmentalized colloidal objects. *Nat. Mater.* **16**, 857–863 (2017).
11. Li, M., Harbron, R. L., Weaver, J. V., Binks, B. P. & Mann, S. Electrostatically gated membrane permeability in inorganic protocells. *Nat. Chem.* **5**, 529–536 (2013).
12. Wu, H., Du, X., Meng, X., Qiu, D. & Qiao, Y. A three-tiered colloidosomal microreactor for continuous flow catalysis. *Nat. Commun.* **12**, 6113 (2021).
13. Dupin, A. & Simmel, F. C. Signalling and differentiation in emulsion-based multi-compartmentalized in vitro gene circuits. *Nat. Chem.* **11**, 32–39 (2019).
14. Tian, D. et al. Multi-compartmental MOF microreactors derived from Pickering double emulsions for chemo-enzymatic cascade catalysis. *Nat. Commun.* **14**, 3226 (2023).
15. Dupin, A. et al. Synthetic cell-based materials extract positional information from morphogen gradients. *Sci. Adv.* **8**, eabl9228 (2022).
16. Yang, Z., Wei, J., Sobolev, Y. I. & Grzybowski, B. A. Systems of mechanized and reactive droplets powered by multi-responsive surfactants. *Nature* **553**, 313–318 (2018).
17. Kumar, B., Patil, A. J. & Mann, S. Enzyme-powered motility in buoyant organoclay/DNA protocells. *Nat. Chem.* **10**, 1154–1163 (2018).
18. Xu, Z., Hueckel, T., Irvine, W. T. M. & Sacanna, S. Transmembrane transport in inorganic colloidal cell-mimics. *Nature* **597**, 220–224 (2021).
19. Kurihara, K. et al. A recursive vesicle-based model protocell with a primitive model cell cycle. *Nat. Commun.* **6**, 8352 (2015).
20. Adamala, K. & Szostak, J. W. Competition between model protocells driven by an encapsulated catalyst. *Nat. Chem.* **5**, 495–501 (2013).
21. Kurihara, K. et al. Self-reproduction of supramolecular giant vesicles combined with the amplification of encapsulated DNA. *Nat. Chem.* **3**, 775–781 (2011).
22. De Franceschi, N., Barth, R., Meindlhumer, S., Fragasso, A. & Dekker, C. Dynamin A as a one-component division machinery for synthetic cells. *Nat. Nanotechnol.* **19**, 70–76 (2024).
23. Zhan, P., Jahnke, K., Liu, N. & Gopfrich, K. Functional DNA-based cytoskeletons for synthetic cells. *Nat. Chem.* **14**, 958–963 (2022).
24. Lee, K. Y. et al. Photosynthetic artificial organelles sustain and control ATP-dependent reactions in a protocellular system. *Nat. Biotechnol.* **36**, 530–535 (2018).
25. Gao, N. et al. Chemical-mediated translocation in protocell-based microactuators. *Nat. Chem.* **13**, 868–879 (2021).
26. Qiao, Y., Li, M., Booth, R. & Mann, S. Predatory behaviour in synthetic protocell communities. *Nat. Chem.* **9**, 110–119 (2016).
27. Joesaar, A. et al. DNA-based communication in populations of synthetic protocells. *Nat. Nanotechnol.* **14**, 369–378 (2019).
28. Mansy, S. S. et al. Template-directed synthesis of a genetic polymer in a model protocell. *Nature* **454**, 122–125 (2008).
29. Bhattacharya, A., Cho, C. J., Brea, R. J. & Devaraj, N. K. Expression of fatty acyl-CoA ligase drives one-pot de novo synthesis of membrane-bound vesicles in a cell-free transcription–translation system. *J. Am. Chem. Soc.* **143**, 11235–11242 (2021).
30. Koga, S., Williams, D. S., Perriman, A. W. & Mann, S. Peptide–nucleotide microdroplets as a step towards a membrane-free protocell model. *Nat. Chem.* **3**, 720–724 (2011).
31. Fares, H. M., Marras, A. E., Ting, J. M., Tirrell, M. V. & Keating, C. D. Impact of wet–dry cycling on the phase behavior and compartmentalization properties of complex coacervates. *Nat. Commun.* **11**, 5423 (2020).
32. Nakashima, K. K., van Haren, M. H. I., Andre, A. A. M., Robu, I. & Spruijt, E. Active coacervate droplets are protocells that grow and resist Ostwald ripening. *Nat. Commun.* **12**, 3819 (2021).
33. Donau, C. et al. Active coacervate droplets as a model for membraneless organelles and protocells. *Nat. Commun.* **11**, 5167 (2020).
34. Abbas, M., Lipinski, W. P., Nakashima, K. K., Huck, W. T. S. & Spruijt, E. A short peptide synthon for liquid–liquid phase separation. *Nat. Chem.* **13**, 1046–1054 (2021).
35. Mashima, T. et al. DNA-mediated protein shuttling between coacervate-based artificial cells. *Angew. Chem. Int. Ed.* **61**, e202115041 (2022).
36. Tian, L. et al. Spontaneous assembly of chemically encoded two-dimensional coacervate droplet arrays by acoustic wave patterning. *Nat. Commun.* **7**, 13068 (2016).
37. Deng, J. & Walther, A. Programmable and chemically fueled DNA coacervates by transient liquid–liquid phase separation. *Chem* **6**, 3329–3343 (2020).
38. Deng, N. N. et al. Macromolecularly crowded protocells from reversibly shrinking monodisperse liposomes. *J. Am. Chem. Soc.* **140**, 7399–7402 (2018).
39. Xu, C., Martin, N., Li, M. & Mann, S. Living material assembly of bacteriogenic protocells. *Nature* **609**, 1029–1037 (2022).
40. Cao, S. et al. Dipeptide coacervates as artificial membraneless organelles for bioorthogonal catalysis. *Nat. Commun.* **15**, 39 (2024).
41. Choi, S., Meyer, M. O., Bevilacqua, P. C. & Keating, C. D. Phase-specific RNA accumulation and duplex thermodynamics in multiphase coacervate models for membraneless organelles. *Nat. Chem.* **14**, 1110–1117 (2022).
42. Mu, W. et al. Superstructural ordering in self-sorting coacervate-based protocell networks. *Nat. Chem.* **16**, 158–167 (2024).
43. Wu, H. & Qiao, Y. Engineering coacervate droplets towards the building of multiplex biomimetic protocells. *Supramol. Mater.* **1**, 100019 (2022).

44. Dora Tang, T. Y. et al. Fatty acid membrane assembly on coacervate microdroplets as a step towards a hybrid protocell model. *Nat. Chem.* **6**, 527–533 (2014).
45. Zhang, Y. et al. Giant coacervate vesicles as an integrated approach to cytomimetic modeling. *J. Am. Chem. Soc.* **143**, 2866–2874 (2021).
46. Mason, A. F., Buddingh', B. C., Williams, D. S. & van Hest, J. C. M. Hierarchical self-assembly of a copolymer-stabilized coacervate protocell. *J. Am. Chem. Soc.* **139**, 17309–17312 (2017).
47. Li, J., Liu, X., Abdelmohsen, L., Williams, D. S. & Huang, X. Spatial organization in proteinaceous membrane-stabilized coacervate protocells. *Small* **15**, e1902893 (2019).
48. Kelley, F. M., Favetta, B., Regy, R. M., Mittal, J. & Schuster, B. S. Amphiphilic proteins coassemble into multiphasic condensates and act as biomolecular surfactants. *Proc. Natl Acad. Sci. USA* **118**, e2109967118 (2021).
49. Ji, Y., Lin, Y. & Qiao, Y. Plant cell-inspired membranization of coacervate protocells with a structured polysaccharide layer. *J. Am. Chem. Soc.* **145**, 12576–12585 (2023).
50. Gao, N., Xu, C., Yin, Z., Li, M. & Mann, S. Triggerable protocell capture in nanoparticle-caged coacervate microdroplets. *J. Am. Chem. Soc.* **144**, 3855–3862 (2022).
51. Liu, S. et al. Enzyme-mediated nitric oxide production in vasoactive erythrocyte membrane-enclosed coacervate protocells. *Nat. Chem.* **12**, 1165–1173 (2020).
52. Zhao, C. et al. Membranization of coacervates into artificial phagocytes with predation toward bacteria. *ACS Nano* **15**, 10048–10057 (2021).
53. Levental, I. & Lyman, E. Regulation of membrane protein structure and function by their lipid nano-environment. *Nat. Rev. Mol. Cell Biol.* **24**, 107–122 (2022).
54. Song, Y. et al. Fabrication of fibrillosomes from droplets stabilized by protein nanofibrils at all-aqueous interfaces. *Nat. Commun.* **7**, 12934 (2016).
55. Bergmann, A. M. et al. Evolution and single-droplet analysis of fuel-driven compartments by droplet-based microfluidics. *Angew. Chem. Int. Ed.* **61**, e202203928 (2022).
56. Rothe G. Technical Background and Methodological Principles of Flow Cytometry (Basel, Karger, 2009).
57. Liang, W. et al. Metal–organic framework-based enzyme biocomposites. *Chem. Rev.* **121**, 1077–1129 (2021).
58. Lyu, F., Zhang, Y., Zare, R. N., Ge, J. & Liu, Z. One-pot synthesis of protein-embedded metal–organic frameworks with enhanced biological activities. *Nano Lett.* **14**, 5761–5765 (2014).
59. Liang, W. et al. Enhanced activity of enzymes encapsulated in hydrophilic metal-organic frameworks. *J. Am. Chem. Soc.* **141**, 2348–2355 (2019).
60. Towne, V., Will, M., Oswald, B. & Zhao, Q. Complexities in horseradish peroxidase-catalyzed oxidation of dihydroxyphenoxazine derivatives: appropriate ranges for pH values and hydrogen peroxide concentrations in quantitative analysis. *Anal. Biochem.* **334**, 290–296 (2004).
61. Yin, Z., Tian, L., Patil, A. J., Li, M. & Mann, S. Spontaneous membranization in a silk-based coacervate protocell model. *Angew. Chem. Int. Ed.* **61**, e202202302 (2022).
62. Garenne, D. et al. Sequestration of proteins by fatty acid coacervates for their encapsulation within vesicles. *Angew. Chem. Int. Ed.* **55**, 13475–13479 (2016).
63. Mason, A. F. et al. Mimicking cellular compartmentalization in a hierarchical protocell through spontaneous spatial organization. *ACS Central Science* **5**, 1360–1365 (2019).
64. Tanner, P. et al. Polymeric vesicles: from drug carriers to nanoreactors and artificial organelles. *Acc. Chem. Res.* **44**, 1039–1049 (2011).
65. Bryant, D. M. & Mostov, K. E. From cells to organs: building polarized tissue. *Nat. Rev. Mol. Cell Biol.* **9**, 887–901 (2008).

Methods

Preparation of MOF-coated PDDA/PAA coacervate microdroplets

Typically, the PDDA/PAA microdroplet dispersions were prepared by mixing 50 µl of PDDA (50 mM, pH 7.0) and 50 µl of PAA solution (50 mM, pH 7.0). Then, 20 µl of PDDA/PAA coacervate suspension was added into 60 µl of MOF nanoparticle dispersion (5.33 mg ml^{-1}) and gently stirred with a pipette tip, followed by incubation for 10 min before characterization.

Measurement of interfacial tension and wetting angle

The interfacial tension was measured by the pendant drop method with a droplet shape analyser (DSA100). Images of pendant coacervate droplets in the coacervate dilute phase and MOF nanoparticle suspension (4 mg ml^{-1}) were captured using a built-in camera, followed by data analysis with Young–Laplace drop shape examination to calculate the interfacial tensions. Briefly, the coacervate phase was loaded in a programmable syringe pump with a vertically mounted needle. The needle was submerged below the liquid level in a glass cuvette containing the coacervate dilute phase or MOF nanoparticle suspension. The coacervate phase was dispensed at 0.5 µl min^{-1} to form a droplet with a volume of 0.4–0.8 µl. The data were analysed with ADVANCE 1.13 software.

The wetting angle was measured by the sitting droplet method using a droplet shape analyser (DSA100). A glass slide was placed in a glass tank with the MOF-coated surface facing upward. The tank was then filled with the dilute phase of the biphasic solution. A coacervate droplet (0.6–1.0 µl) was subsequently deposited onto the slide surface and the image was captured using the built-in camera. The data were analysed with ADVANCE 1.13 software.

Flow cytometry

The membrane-bound or membraneless coacervate dispersions were prepared by the above methods and characterized with an ACEA Novocyte flow cytometer. The flow speed was set to be 7 µl min^{-1}, and the 2D pseudocolour plots were determined for a total volume of 10 µl. Data were analysed with FlowJo 10.4 software.

FRAP experiments

In a FRAP experiment, photobleaching was performed by exposing the region of interest (ROI) to a 100% power laser beam, and the fluorescence recovery was monitored with a 5% power laser beam. A CLSM (Olympus FV1000-IX81, iXon camera, ×100 oil immersion lens) equipped with a 488-nm laser (for coacervate lumen) and a 559-nm laser (for MOF membrane) was used to bleach the ROI for 1 s and 6 s, respectively. The fluorescence microscopy images were collected every 18 s (for coacervate lumen) and 60 s (for MOF membrane) for fluorescence recovery analysis. The apparent diffusion coefficient (D_{app}) was calculated using the equation $D_{app} = \frac{r^2}{t}$, where t is the recovery time after photobleaching and r is the radius of ROI.

Regulation of the enzymatic cascade reaction

For the GOx@MOF- and HRP@MOF-catalysed oxidation of Amplex red, 0.5 µl of Amplex red (250 µM in DMSO) was added to 50 µl of prepared PDDA/PAA coacervate dispersion (total concentration, 12.5 mM; molar ratio, 1:1) coated with GOx@MOF and HRP@MOF nanoparticles (total concentration, 5.33 mg ml^{-1}; mass ratio, 1:1). Then, 1 µl of glucose solution (50 mM) was added into 20 µl of the above mixture to initiate the reaction, and the fluorescence intensity from resorufin was recorded by CLSM (Zeiss LSM880) every 5 s.

For the reaction of GOx/HRP-mediated oxidation of Amplex red, 1 µl of GOx (0.5 mg ml^{-1}) and HRP (0.5 mg ml^{-1}) mixed solution, and 0.5 µl of Amplex red (250 µM in DMSO) was added to 50 µl of PDDA/PAA coacervate dispersion (total concentration, 12.5 mM; molar ratio, 1:1) with or without coating with MOF nanoparticles (final concentration, 4 mg ml^{-1}). Then, 1 µl of glucose solution (50 mM) was added into 20 µl of the above mixture to initiate the reaction, and the fluorescence intensity from the intermediate of resorufin was recorded by CLSM (Zeiss LSM880) every 5 s.

For the lipase-mediated lysis of FDA, 1 µl of lipase solution (10 mg ml^{-1}) was added to 50 µl of PDDA/PAA coacervate dispersion (total concentration, 12.5 mM; molar ratio, 1:1) with or without MOF nanoparticles (final concentration, 4 mg ml^{-1}). Then, 1 µl of FDA (0.5 mg ml^{-1}) was subsequently added to 20 µl of MOF-coated coacervate dispersion to initiate the reaction. The fluorescence increase from the production of fluorescein was recorded by CLSM (Zeiss LSM880, Germany) every 5 s.

Construction of MOF-coated multicompartmentalized coacervates

Typically, the Prot/FA coacervates were prepared by mixing 20 µl of FA (11.08 mg ml^{-1}, 25 mM, pH 10.0) with 60 µl of Prot solution (4.25 mg ml^{-1}, monomer concentration, 25 mM, pH 10.0). Then, 4 µl of Prot/FA coacervates was mixed with 100 µl of PDDA/PAA coacervates with strong stirring to form multiphase coacervates. Next, 40 µl of Prot/FA@PDDA/PAA coacervate dispersion was added into 60 µl of MOF nanoparticle dispersion (5.33 mg ml^{-1}), followed by gentle stirring with a pipette tip and incubation for 10 min. Similarly, the Prot/DNA organelle was prepared by mixing 80 µl of Prot (4.25 mg ml^{-1}, pH 7.0) with 20 µl of DNA solution (10 mg ml^{-1}, pH 7.0); the vesicle-like Prot/FA organelle was prepared by mixing 100 µl of Prot (25 mM, pH 10.0) with 10 µl of FA (25 mM, pH 10). Prot/FA organelles with different catalytic functions were encapsulated with FITC-GOx (12.5 µg ml^{-1}) or Cy5-HRP (12.5 µg ml^{-1}). Then, 4 µl of the as-prepared organelles were added into 100 µl of the PDDA/PAA coacervates with strong stirring, followed by surface coating with MOF membrane.

Cascade enzymatic reaction in MOF-coated multicompartmentalized coacervates, binary coacervate populations and multiphase coacervates

For the MOF-coated multicompartmentalized coacervates and multiphase coacervates, 8 µl of Prot/FA coacervates containing 0.5 mg ml^{-1} GOx and 0.5 mg ml^{-1} HRP (doped with 10% FITC-HRP) was mixed with 100 µl of PDDA/PAA coacervates containing 0.5 mg ml^{-1} amylase. The mixture was stirred strongly to form multiphase coacervates. In addition, the multiphase coacervates were coated with ZIF-8 to form MOF-coated multicompartmentalized coacervates. For the binary coacervate populations, 8 µl of membraneless Prot/FA coacervates containing 0.5 mg ml^{-1} GOx and 0.5 mg ml^{-1} HRP (doped with 10% FITC-HRP) was mixed with 100 µl of MOF-coated PDDA/PAA coacervates containing 0.5 mg ml^{-1} amylase. Subsequently, 2.5 µl of Amplex red (250 µM in DMSO) was added into 100 µl of the MOF-coated multicompartmentalized coacervates or the binary coacervate populations and equilibrated for 5 min; then, 40 µl of each sample was added to the glass slide. The enzymatic reactions were initiated with the addition of 1 µl of 10 mg ml^{-1} amylose into the sample cell and the fluorescence change was monitored by CLSM (Zeiss LSM880) every 10 s.

Construction of prototissues with MOF-coated coacervates

Typically, 80 µl of MOF-coated coacervate dispersion was added into the glass cell and allowed to settle for 10 min to obtain high-density MOF-coated coacervates; then, 50 µl of supernatant was removed. The prototissues were formed by adding 1 µl of 0.1-M sodium chloride solution into the glass cell to promote the assembly of MOF-coated coacervates.

Chemical communications in the prototissues

For the prototissues with enzymes in artificial organelles, β-gal (25 µg ml^{-1}, doped with 10% FITC-β-gal), GOx (12.5 µg ml^{-1}, doped with 10% RITC-GOx) or HRP (12.5 µg ml^{-1}, doped with 10% Cy5-HRP) were sequestered individually by the Prot/FA organelles within MOF-coated

multicompartmentalized coacervates. Then, 50 µl of the mixed MOF-coated multicompartmentalized coacervate populations was used to build ternary prototissues according to the above protocol. Subsequently, 0.5 µl of Amplex red (250 µM in DMSO) was added into the sample cell and equilibrated for 5 min, followed by pipetting 1 µl of 500-mM lactose to initiate the reaction. The fluorescence change was recorded by CLSM (Zeiss LSM880) every 10 s.

For the prototissues with relocated enzymes on the membrane, β-gal (25 µg ml^{-1}, doped with 10% FITC-β-gal), GOx (12.5 µg ml^{-1}, doped with 10% RITC-GOx) or HRP (12.5 µg ml^{-1}, doped with 10% DL405-HRP) containing membrane-bound coacervates were prepared individually. Then, 50 µl of the mixed MOF-coated coacervate populations was used to build ternary prototissues according to the above protocol. Subsequently, 0.5 µl of Amplex red (250 µM in DMSO) was added into the sample cell and equilibrated for 5 min, followed by pipetting 1 µl of 500-mM lactose to initiate the reaction. The fluorescence change was recorded by CLSM (Zeiss LSM880) every 10 s.

Data availability

All data needed to evaluate the conclusions in the paper are present in the paper and/or the Supplementary Information. Source data are provided with this paper.

Acknowledgements

We thank the National Natural Science Foundation of China (T2425001 and 22172007), the Strategic Priority Research Program of the Chinese Academy of Sciences (XDB0480000 and XDB0960000), the Beijing Natural Science Foundation (JQ24008), the CAS Youth Interdisciplinary Team, the National Key R&D Program of China (2023YFC2507000), the Science Fund for Creative Research Groups of the National Natural Science Foundation of China (52221006) and the Fundamental Research Funds for the Central Universities (buctrc202015) for financial support.

Author contributions

Y.Q. led the project. Y.J. performed the experiments. Y.J. and Y.Q. conceived the experiments. Y.J., Y.L. and Y.Q. analysed the data and wrote the manuscript. All authors discussed the results and have given approval to the final version of the manuscript.

Competing interests

The authors declare no competing interests.

Additional information

Supplementary information The online version contains supplementary material available at https://doi.org/10.1038/s41557-025-01827-7.

Correspondence and requests for materials should be addressed to Yan Qiao.

Peer review information *Nature Chemistry* thanks Lucas Caire da Silva, Alexander Mason and the other, anonymous, reviewer(s) for their contribution to the peer review of this work.